ACS APPLIED MATERIALS & INTERFACES

Research Article

www.acsami.org

Morphology Defects Guided Pore Initiation during the Formation of Porous Anodic Alumina

Jie Yang,[†,‡,⊥] Hongtao Huang,[‡,⊥] Qingfeng Lin,[§] Linfeng Lu,[‡] Xiaoyuan Chen,[‡] Liyou Yang,[‡] Xufei Zhu,[†] Zhiyong Fan,*[,§] Ye Song,*[,†] and Dongdong Li*[,‡]

[†]School of Chemical Engineering, Nanjing University of Science and Technology, Nanjing, Jiangsu 210094, China

[‡]Shanghai Advanced Research Institute, Chinese Academy of Sciences, Shanghai 201210, China

[§]Department of Electronic and Computer Engineering, Hong Kong University of Science and Technology, Hong Kong, China

Supporting Information

ABSTRACT: Aluminum (Al) anodization leads to formation of porous structures with a broad spectrum of applications. Naturally or intentionally created defects on Al surfaces can greatly affect pore initiation. However, there is still a lack of systematic understanding on the defect dependent morphology evolution. In this paper, anodization processes on unpolished, polished, and nanoimprinted Al substrates are investigated under high voltages up to 600 V in various acid solutions. A porous structure is obtained on the unpolished and nanoimprinted Al foils with rough surface texture, whereas a compact film can be rationally obtained on the polished Al foil with a highly smooth surface. The observation of surface roughness dependent oxide film morphology evolution could be originated from the high voltages, which increases the threshold requirement of defect size or density for the pore initiation. Electrostatics simulation results indicate that inhomogeneous electric field and its corresponding localized high current induced by the surface roughness facilitate the initiation of nanopores. In addition, the porous films are utilized as templates to produce polydimethylsiloxane nanocone and submicrowire arrays. The nanoarrays with different aspect ratios present tunable wettability with the contact angles ranging from 144.6° to 56.7°, which hold promising potentials in microfluidic devices and self-cleaning coatings.

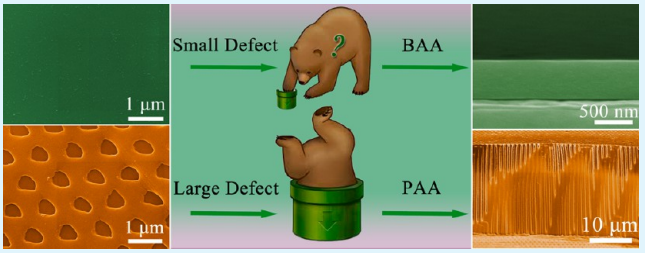

KEYWORDS: *anodic alumina, porous-type, barrier-type, surface roughness, electric field, wettability*

1. INTRODUCTION

Self-organized porous anodic alumina has been widely investigated both in the fundamental understanding of the self-organizing mechanism[1−4] and the extensive applications.[5−11] Some mechanisms such as field-assisted dissolution,[4,12,13] oxide flow model,[14,15] and oxygen bubble mold[16,17] have been proposed with respect to the formation of such porous structure. Experimental results showed that acid solutions induce the formation of porous-type anodic alumina (PAA), while the barrier-type anodic alumina (BAA) can only be obtained in neutral solution, which is independent of the aluminum surface morphologies.[18,19] It is commonly accepted that the porous structures are initiated by roughening of the oxide/electrolyte (O/E) interface during anodization.[13] Oh and Thompson proposed that the mechanical instability in the oxide film accounts for the initial roughening of the oxide film at O/E interface.[3] At valleys of the O/E interface, the electric field is concentrated, which facilitates the pore initiation either by field-assisted dissolution or oxide flow.

The nanoimprint method has been developed to produce porous alumina films with precisely controlled size and shape.[20−23] As such, nanoimprint produces intentionally defined defects on the Al substrate surface, and the defects affect the surface electric field distribution during anodization of the Al substrate. However, there is a lack of systematic understanding on how the defect and the electric field distribution determine pore initiation in the beginning of the anodization process. Recently, Yu et al. found an interesting morphology evolution that loosely packed nanotube arrays with many visible voids were obtained on unpolished Al foil, whereas a more closely packed structure was obtained on polished smooth Al foil.[24] In this study, anodizing behaviors on Al substrates with different surface morphologies (i.e. unpolished samples with naturally formed surface grooves during rolling process, polished samples with smooth surface, and imprinted ones with periodic depressions) are investigated to clarify the relationship between surface morphology of Al and pore initiation in the oxide layer. Interestingly, BAA film can be rationally obtained on the polished Al substrate, whereas unpolished and nanoimprinted substrates with a rough surface provide suitable platforms for the formation of PAA. A defects guided manner to the formation of porous structures is

Received: August 13, 2013
Accepted: January 28, 2014
Published: January 28, 2014

   dx.doi.org/10.1021/am405294x | ACS Appl. Mater. Interfaces 2014, 6, 2285−2291

proposed through careful analysis of the unusual results and electrostatics simulations, which may provide a new insight into structural engineering of anodic alumina and understanding the growth kinetics of other anodic films.[25] As a demonstration for template application, flexible nanoarray membranes with tunable wettability are subsequently constructed by filling polydimethylsiloxane (PDMS) into the hexagonal close-packed PAA films.

2. EXPERIMENTAL SECTION

Aluminum foils (0.3 mm thickness, 99.999% purity) are ultrasonically cleaned in acetone, ethanol, and deionized water each for 15 min and dried in ionized nitrogen flow. A part of the foils is then electropolished in a mixture of perchloric acid and ethanol (1:3 in volume) under 10 V and 5 °C for 8 min to form a flat and mirror-like surface. Subsequently, a silicon nanostamp with hexagonal array of nanopillars (1 μm in pitch, 100 nm in depth, 500 nm in width, LightSmyth Technologies) is employed as the mother mold to produce ideally ordered nanoconcave arrays on polished foils under a pressure of 1.1×10^4 N cm^{-2}.[21]

The following anodization experiments are carried out on these Al foils with different surface morphologies, namely, unpolished samples with naturally formed grooves during rolling process, polished samples with smooth surface, and imprinted ones on polished foils with periodic hexagonal depressions. These anodizing processes are consistently performed in a mixture of 0.1 wt % phosphoric acid aqueous solution, 4 wt % citric acid aqueous solution, and ethylene glycol (1:10:10 in volume, pH ~2.5) under 400 V at constant temperature 10 °C with 800 rpm stirring for 20,000 s. The purpose of employing the specific voltage is to follow the empirical rule of 2.5 nm/V (interpore distance/applied voltage) in view of the pattern size of the silicon mold. Furthermore, anodization in citric acid (4 wt % aqueous solution with pH ~1.5) under 240, 300, and 400 V, and oxalic acid (0.3 M aqueous solution diluted by ethanol (1:8 in volume)) under 400, 500, and 600 V is also carried out to elucidate the defects induced morphology transition.

Highly ordered hexagonal PAA (pitch size 1 μm) films are used as templates to prepare PDMS nanoarrays with different aspect ratios. Two batches of PAA membranes (0.5 μm and 20 μm channel length) are placed in 5 wt % phosphoric aqueous solution for pore broadening (15 min). PDMS slurry, prepared by mixing the sylgard 184 PDMS prepolymer and the cross-linking agent (10:1, w:w), is then poured onto the PAA templates. After that, the composite membranes are solidified at 60 °C in a vacuum drying oven for 3 h. The oxide film together with Al foil is then thoroughly removed by chemical etching in 1 M NaOH for 30 min, and only PDMS membranes decorated with nanoarrays are left. Then wettability of the PDMS membranes is evaluated with respect to the aspect ratios of nanoarrays and oxygen plasma treatments. Oxygen plasma treatments are conducted in Plasma-Preen II-862 (Plasmatic Systems, 2 Torr O_2, 80 W) for 60 s.

The current-time curves during anodization are recorded by a Keithley 2612A sourcemeter. The morphologies of Al foils and as-prepared anodic aluminum oxide membranes are characterized by field-emission scanning electron microscopy (FESEM, NOVA Nano SEM 230) and atomic force microscopy (AFM, Dimension Icon, Bruker Corporation), respectively. The 3-D electric field distribution is simulated using COMSOL Multiphysics software. The contact angles of PDMS membranes are measured by using a Kruss Kontaktwinkel DSA100 setup.

3. RESULTS AND DISCUSSION

Figure 1a-c displays the surface morphologies of the three different Al foils as discussed above. It is obvious that electropolishing has successfully removed the groove characteristics and given rise to a smooth surface (Figure 1b). The following nanoimprinting process yields well-defined hexagonal nanoconcave arrays (Figure 1c).

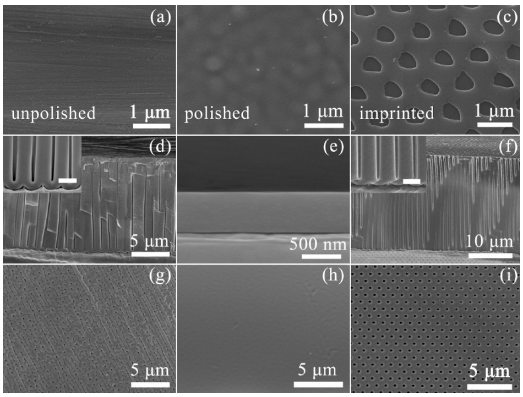

Figure 1. SEM images of Al foils: (a) raw materials, (b) polished, and (c) nanoimprinted samples. SEM images of (d-f) cross-sectional and (g-i) surface morphologies of the oxide films obtained from Al foils with different pretreatments: (d, g) unpolished, (e, h) polished, (f, i) nanoimprinted. The insets in (d) and (f) are magnified views at the bottom of PAA membranes. Scale bars of the insets represent 1 μm.

The cross-sectional and surface morphologies of as-obtained oxide films present a remarkable difference. Figure 1d and g illustrates the typical PAA films with a thickness of ~12.5 μm. The formation sites of nanopores follow the stripe-like grooves on the unpolished sample. Unexpectedly, a typical BAA film with a thickness of ~520 nm is formed on the polished Al foil (Figure 1e and h) under the same anodizing condition, which inherits the smooth surface of the polished foil. The distinct morphology difference of the oxide films formed on unpolished and polished foils indicates that the morphological fluctuation plays a crucial role on the pore initiation. In addition, the thickness of BAA film abides by the ~1.3 nm/V (oxide layer thickness/applied voltage: 520 nm/400 V) rule of "mild anodization".[26] However, the ratio of barrier layer thickness to anodization voltage (~1.0 nm/V) in PAA is 20% lower, showing a "hard anodization" characteristic.[26] Considering the applied voltage (400 V) is much higher than the reported breakdown voltage in citric acid (245 V),[27] this could be ascribed to the relatively high current density involved in the anodization process in accordance with the high field conductivity theory.[2,13,26]

A more straightforward evidence of the defects guided process can be found based on the substrates with artificially pre-defined nanoconcaves (Figure 1c). As expected, a PAA film (with a thickness of ~21.5 μm, Figure 1f) is obtained due to the existence of nanoconcave arrays. More importantly, the pre-patterned nanoconcaves exactly guide the growth of nanopores, resulting in ideally ordered arrays (Figure 1i). This morphology transition provides strong evidence that entirely different types of oxide films (PAA and BAA) can be obtained under the same anodizing conditions, being strongly dependent on the surface morphology and roughness.

The transitional regions of the nanoimprinted/polished surface are shown in Figure 2a, where a transition from highly ordered PAA, to irregular PAA, and finally to BAA can be observed. In the well pre-patterned area (Figure 2b), the PAA holes are arranged in ordered hexagons. Outside the imprinted region, there is the BAA film formed on the polished Al foil surface (Figure 2d). Between these two areas (Figure 2c), a transition zone exists, where PAA is also obtained but the nanopores are irregularly distributed. This morphology transition is also strong evidence that totally different kinds

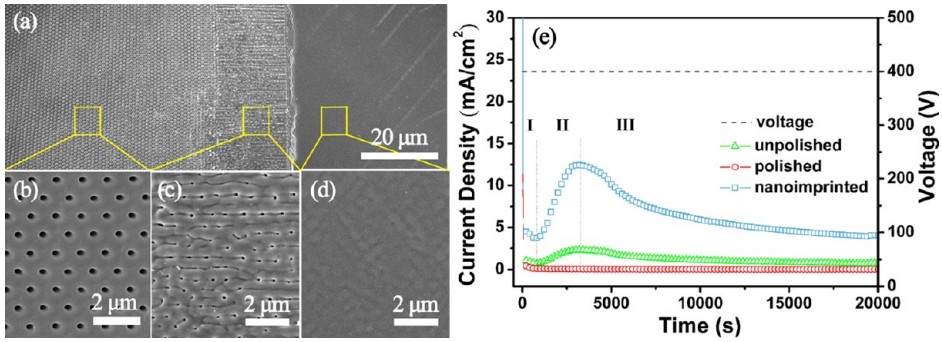

Figure 2. (a) SEM image of anodic alumina at the edge of the nanoimprinted region and polished surface. (b-d) magnified SEM images of labeled boxes in (a). (e) Anodizing current density transients during the anodization on three Al foils with different morphologies under 400 V bias voltage.

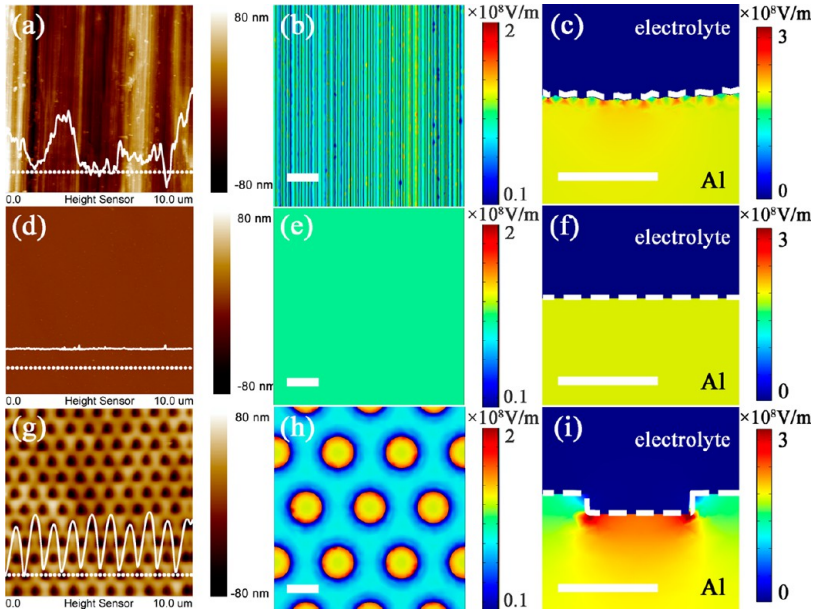

Figure 3. (a, d, g) AFM images and electric field distribution (b, e, h) on the surface and (c, f, i) on the cross-sections of Al foils with different pretreatments: (a-c) unpolished, (d-f) polished, (g-i) nanoimprinted. The scale bars represent 500 nm.

of oxide films can be conveniently controlled with tunable surface morphology and roughness.

Figure 2e shows the current density versus time (*j-t*) transients under 400 V. The *j-t* curves for unpolished and nanoimprinted samples show a typical three-stage feature in the porous film growth.[12,18,28] The current density decreases rapidly in stage I, rises up in stage II with an overshoot, and reaches a steady state in stage III. In the case of the polished sample, the current density reaches steady state directly after the initial sharp decline without any rebound, which follows the typical growth characteristics of BAA films.[19,28] These observations match well with the traditional empirical results.[12,18]

In order to further interpret the growth mechanisms of the oxide membranes, AFM measurements are conducted to record surface characteristics of the different Al foils. The surface roughness (R_q) of the unpolished foil reaches 36.7 nm (Figure 3a), while electropolishing reduces the value down to 0.78 nm (Figure 3d). The following nanoimprinting process on the polished substrate increases the roughness back to 23.1 nm (Figure 3g), and the average width and depth of the nanoimprinted depressions are measured to be ~500 nm and ~100 nm, respectively, in accordance with the dimensions of silicon mold. Simplified three-dimensional simulations are performed by referring to the AFM results in 3 × 3 μm^2 to elucidate electric field distributions. In this simulation, we mainly focus on the electric field distribution in the metallic layer at the very initial stage (i.e. no oxide film formed yet) based on steady-state current continuity equation, excluding the electrolyte concentration gradient and the electrode double layer at the electrolyte/electrode interface.[2]

The simulation results demonstrate that the polished sample has a uniform electric field distribution and relatively low strength (1.0×10^8 V/m) over the entire surface (Figure 3e and f, Figure S1). In contrast, the unpolished and nanoimprinted samples show a nonuniform electric field distribution as illustrated in Figure 3b, c, h, and i. Figure S1d reveals that the highest electric field strength (1.75×10^8 V/m) locates at the corners of the concave bottom on the prepatterned substrate. This predefined electric field strength distribution will benefit the initiation and growth of porous film and eventually lead to a close-packed array of columnar hexagonal cells.[2,15] The much enhanced electric field on the nanoimprinted sample in comparison with that of the unpolished foil (see Figure 3c and i) may explain the higher current density (Figure 2e) and the corresponding higher growth rate (deduced from different

dx.doi.org/10.1021/am405294x | ACS Appl. Mater. Interfaces 2014, 6, 2285−2291

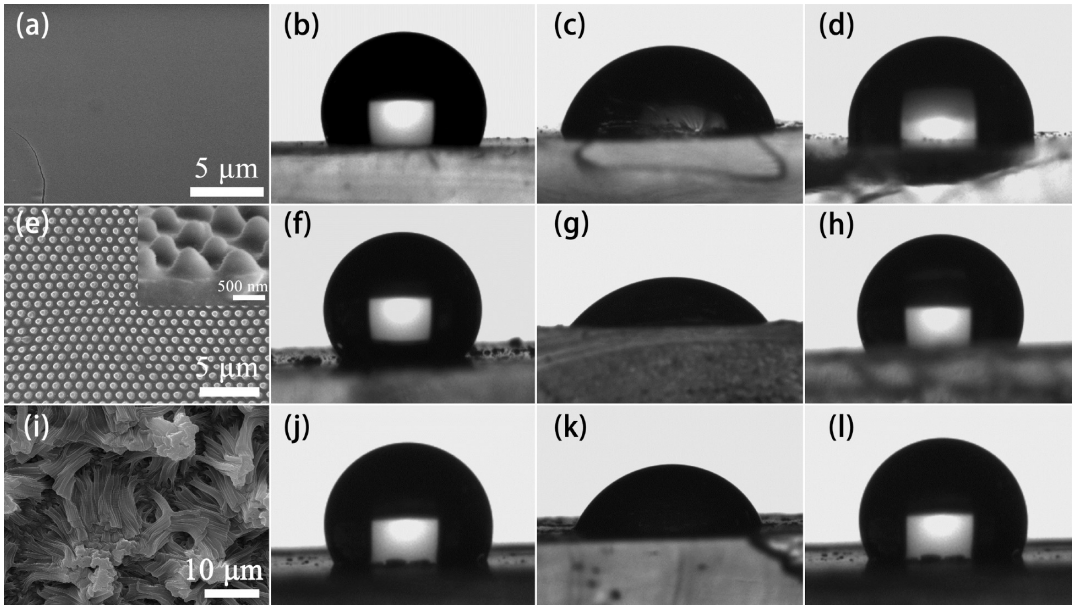

Figure 4. SEM images of PDMS membranes with different surface morphologies: (a) planar PDMS, (e) nanocones PDMS and (i) submicrowires PDMS. Contact angle on PDMS membranes with tunable wettability: (b, c, d) planar PDMS, (f, g, h) nanocones PDMS, and (j, k, l) submicrowires PDMS. (b, f, j) original membranes, (c, g, k) membranes right after oxygen plasma treatment, (d, h, l) membranes after oxygen plasma treatment and 40 h of aging in ambient atmosphere.

thicknesses of ~12.5 μm and ~21.5 μm shown in Figure 1d and f). The electric fields within the oxide layers (20 nm in thickness) forming at the beginning of anodization are also simulated as shown in Figure S2. The fluctuations of field strength within oxides on unpolished and imprinted Al foils are also much larger than that on polished Al.

The field-assisted dissolution model and dissolution current cannot explain the rise of current in stage II of Figure 2e.[12,19,29] The dissolution reaction ($Al_2O_3 + 6H^+ \rightarrow 3H_2O + 2Al^{3+}$) only takes place at the electrolyte/oxide interface, which cannot supply charge carriers to establish a conductive path between two interfaces (electrolyte/oxide and oxide/Al interfaces).[29] That is to say, the so-called dissolution current across the barrier oxide layer is impossible to be formed.[29]

Here, the total anodic current (J_t), composed by ionic current (J_{ion}) and electronic current (J_e), is taken into account to interpret the unusual morphologies evolution. We have proposed that the formation of oxide film is determined by J_{ion}, and J_e gives rise to the evolution of oxygen gas which is responsible to the pore formation.[2,16,17,28]

The ionic current (J_{ion}) and the electric field strength (E) are related through the exponential law[13,19]

$$J_{ion} = Ae^{BE} \quad (1)$$

where A and B are temperature-dependent constants involving parameters of ionic transport. The relation between J_e and the barrier layer thickness t_b can be expressed as[28]

$$J_e = J_{e0} \exp(\theta t_b) \quad (2)$$

where J_{e0} is the primary electronic current. θ is the impact ionization coefficient which has a negative value.

In the initial stage (stage I), the formation of the initial oxide film leads to the increase of t_b and the reduction of E, so both J_{ion} and J_e as well as the total current J_t decrease rapidly, according to eqs 1 and 2. However, the morphologies of initial oxide films on unpolished/imprinted and polished Al foils are different. The uneven E on unpolished/imprinted Al foils creates inhomogeneous J_{ion} (eq 1), which is responsible to the nonuniformity of initial oxide film thickness. On the contrary, the homogeneous E on polished Al foil creates a uniform initial oxide film. This difference plays an important role in stage II and the morphologies of final oxide films. When the thickness of initial oxide film grows to a critical value at the end of stage I, there exists a gradient of initial oxide film thickness on unpolished/imprinted Al foils. This gradient leads to the flow of oxide material from the high-field spots to low-field regions, according to the oxide flow model.[12−15] Consequently, the oxide film thickness t_b decreases at the high-field spots, leading to the increase of E. As a result, both J_{ion} and J_e as well as the total current J_t increase in stage II (according to eqs 1 and 2). The increased J_e also releases large amounts of oxygen bubbles. These bubbles guide the flow of oxide material and lead to the initiation of nanopores and the formation of PAA.[2] The rise of J_{ion} accelerates the formation of oxide material, which, in turn, suppresses the increase of current.[16] Finally, the thickness of barrier layer, the current, and the electric field reach a dynamic balance in stage III. As to the polished Al foil, the gradient of initial oxide film thickness is so small due to the homogeneous electric field, that it cannot facilitate the flow of oxide material. Thus the thickness of oxide film keeps uniform during the whole anodization process and BAA forms. When the film grows thicker, the current continues to decrease as well as the film growth rate. Eventually, the thickness of BAA reaches a limit with respect to the constant value of 1.3 nm/V.

These findings deviate from the general perception that acid solutions always generate PAA films no matter whether the Al foil is polished or not.[18,30] In order to confirm that the morphological defects guided pore initiation is not a special case in this kind of electrolyte, anodization is also conducted in more frequently-used acidic solutions. Figure S3 shows the morphologies of oxide films anodized in 4 wt % citric acid aqueous solution[30] (pH ~ 1.5) under 300 V and 400 V. The unpolished Al foils still result in PAA films (Figure S3a and c),

while BAA films (Figure S3b and d) are obtained on the polished Al foils under the same conditions. The same results are also observed in diluted oxalic acid solutions (0.3 M aqueous solution diluted by ethanol (1:8 in volume)) under 500 V and 600 V as shown in Figure S4a-d. Chu et al. have also reported this morphology evolution in malic acid solutions.[30] In their experiments conducted in 2 wt % malic acid with a fixed voltage of 450 V, PAA and BAA are obtained on Al foil with naturally formed grooves and sputtered Al film on FTO/glass substrate with a smooth surface, respectively. They attributed the formation of barrier-type films to the temperature increase caused by the Joule heat produced at the ultrahigh anodizing potential. The increased temperature may enhance the dehydration of aluminum hydroxides and lead to a compact alumina, thus hindering the pore generation or pore growth, or both, thereafter. However, this hypothesis can hardly explain the different oxide morphologies obtained on polished and unpolished/imprinted Al foils, which have the same thermal conductivity. Our analysis based on morphology guided initiation provides a more reasonable explanation to this phenomenon.

Another interesting phenomenon is that both unpolished and polished Al foils result in PAA in oxalic acid when the voltage drops from 500 V to 400 V (Figure S4e and f). Similarly, the BAA obtained in citric acid transforms to PAA when the voltage decreases to 240 V as shown in Figure S5. This indicates that the key point to observe BAA on polished Al foil is the much higher anodization voltage than the conventional conditions. To initial the formation of nanopores, larger defects are required under higher voltages. These larger defects are usually removed during the polishing process, so BAAs are obtained on polished Al foils under high voltages, rather than PAAs. However, smaller defects still remain on polished Al foils, which are sufficient to create electric field inhomogeneity and initial the pore formation under lower voltages. The conventional anodization voltages in sulfuric,[31] oxalic,[31] phosphoric,[31] citric acid,[27] and malonic acid[32] solutions are usually lower than the critical voltages required to form BAA. That could be the reason why we rarely observe BAA under general anodization conditions.

Since PAA is one of the most popular templates for various functional materials, we use the ordered PAA as a demonstration for template application to produce PDMS nanoarrays with highly tunable wettability. The surface of planar PDMS (Figure 4a) is naturally hydrophobic with a contact angle of 113.8 ± 1.7°, as shown in Figure 4b. Oxygen plasma treatments are usually used to modify the wettability of PDMS for applications like microfluidic devices.[33] The surface of PDMS can be oxidized under the plasma treatment, leading to the formation of polar chemical species such as silanol groups (Si−OH).[34] These polar groups make the exposed surface hydrophilic.[33,34] This change can be observed through the contact angle which decreases to 73.7 ± 2.1° (Figure 4c). The hydrophilic characteristic of PDMS tends to revert to their original hydrophobic states caused by the diffusion of low-molecular-weight chains from the bulk PDMS to the oxidized surface.[35] As shown on the planar PDMS, the contact angle recovers to 99.7 ± 0.8° (Figure 4d) after aging for 40 h in ambient atmosphere. Notably, the tuning range of contact angle on planar PDMS is limited to ~40.1°, which somewhat restricts the application of PDMS.

Patterned by the highly ordered PAA, nanocone arrays (~500 nm in height) are obtained on the surface of PDMS as shown in Figure 4e. This submicrometer scale structure topographically enhances the basic wetting behavior of the surface and extends the tuning range of contact angle. Before oxygen plasma treatment, it is a Cassie-type[36] surface owing to a high enough aspect ratio of about 1 which is much larger than the critical value calculated according to the equation estimated by Extrand.[37] The water droplet does not touch the floor of the nanocones but effectively sits upon a composite surface of the protrusions and air. This situation significantly increases the contact angle up to 141.7 ± 2.3° (Figure 4f), leading to an improved hydrophobicity feature as compared with planar surface. The nanocone arrays also turn to be hydrophilic after the oxygen plasma treatment, showing a much smaller contact angle of 56.7 ± 1.9° (Figure 4g) than that of the flat PDMS surface. The surface free energy contributed by the solid-liquid interface and solid-vapor interface is documented to increase on a rough surface by Wenzel's model, where a smaller contact angle is achieved on a hydrophilic surface due to the increased surface area.[38] After aging for 40 h, the contact angle of nanocones surface recovers to 117.7 ± 2.4° (Figure 4h).

Furthermore, submicrowire arrays (~20 μm in length) with a larger aspect ratio are also investigated using thicker PAA as the template. As shown in Figure 4i, the submicrowires collapse into an entangled mat due to the low elastic modulus of PDMS,[39] resulting in a hierarchical structure with bundled submicrowires. This architecture with dual-scale roughness has been expected to increase the contact angles.[40] The measured results show that the contact angle reaches as high as 144.6 ± 2.9° (Figure 4j) and then decreases to 72.5 ± 3.3° (Figure 4k) after exposed in the oxygen plasma. The recovered contact angle is 109.1 ±3.5° (Figure 4l) after aging for 40 h. The contact angles on different PDMS surfaces are summarized in Table S1. In short, the as-prepared PAA templates show the capability to produce nanostructured PDMS membranes with an extended tuning range of contact angles from 144.6° to 56.7°, which holds promising potentials in microfluidic devices and self-cleaning coatings.

4. CONCLUSIONS

In summary, both the porous and barrier-type anodic alumina films have been achieved in identical electrolytesand anodization voltages. The morphology evolution is strongly determined by the surface roughness of Al foils. Anodization performed on the electropolished Al foil with smooth surface produces a dense oxide film, arising from the uniform electric field and current distribution. The naturally formed grooves on the unpolished samples and intentionally introduced periodic depressions on the imprinted ones serve as the initial formation sites and yield porous oxide films, which is ascribed to the localized high electric field and the corresponding high current density. Moreover, the nanoimprinting technique facilitates porous films with well-defined size, shape, and arrangement. In the end, PAA with a close-packed array of columnar hexagonal cells have been demonstrated as templates to fabricate PDMS nanocone and submicrowire arrays. With the assistance of plasma treatment, the contact angles can be rationally tailored from 144.6° to 56.7°. The inexpensive and durable pattern replication approach based on transparent and flexible PDMS membranes holds great potential for many scientific and engineering applications such as lab-on-a-chip devices, nanophotonics, and self-cleaning coatings.

■ ASSOCIATED CONTENT

Supporting Information

The electric field profiles on unpolished, polished, and imprinted Al foils; the electric field distributions within the initial oxide films on unpolished, polished, and imprinted Al foils; the SEM images of PAA and BAA prepared under 300 V and 400 V in 4 wt % citric acid solution; the SEM images of PAA and BAA prepared in diluted oxalic acid solution; the SEM image of PAA obtained on polished Al foil in 4 wt % citric acid under 240 V; and the table of contact angles on different PDMS surfaces. This material is available free of charge via the Internet at http://pubs.acs.org.

■ AUTHOR INFORMATION

Corresponding Authors

*E-mail: eezfan@ust.hk (Z.F.).
*E-mail: soong_ye@sohu.com (Y.S.).
*E-mail: lidd@sari.ac.cn (D.L.).

Author Contributions

⊥These authors contributed equally.

Notes

The authors declare no competing financial interest.

■ ACKNOWLEDGMENTS

The authors acknowledge technical assistance on COMSOL simulations from Dr. Liang Zhao from Stanford University and Dr. Paul W. Leu from University of Pittsburgh, USA. This work was financially supported by the National Natural Science Foundation of China (61171043, 51077072, 51102271), the Science & Technology Commission of Shanghai Municipality (13DZ1106000), the Natural Science Foundation of Shanghai (11ZR1436300), the Shanghai Municipal Human Resources and Social Security Bureau (2011033), Hong Kong Innovation Technology Commission (ITS/192/11), Hong Kong Research Grant Council (GRF 612111), and National Research Foundation of Korea (NRF-2010-220-D00060, 2008-0662256).

■ REFERENCES

(1) Hebert, K. R.; Albu, S. P.; Paramasivam, I.; Schmuki, P. Morphological Instability Leading to Formation of Porous Anodic Oxide Films. *Nat. Mater.* **2012**, *11*, 162−166.

(2) Li, D.; Zhao, L.; Jiang, C.; Lu, J. G. Formation of Anodic Aluminum Oxide with Serrated Nanochannels. *Nano Lett.* **2010**, *10*, 2766−2771.

(3) Oh, J.; Thompson, C. V. The Role of Electric Field in Pore Formation During Aluminum Anodization. *Electrochim. Acta* **2011**, *56*, 4044−4051.

(4) Reis, F. D. A. A.; Badiali, J. P.; di Caprio, D. Modeling Growth of Organized Nanoporous Structures by Anodic Oxidation. *Langmuir* **2012**, *28*, 13034−13041.

(5) Lee, S. B.; Mitchell, D. T.; Trofin, L.; Nevanen, T. K.; Söderlund, H.; Martin, C. R. Antibody-Based Bio-Nanotube Membranes for Enantiomeric Drug Separations. *Science* **2002**, *296*, 2198−2200.

(6) ter Maat, J.; Regeling, R.; Ingham, C. J.; Weijers, C. A. G. M.; Giesbers, M.; de Vos, W. M.; Zuilhof, H. Organic Modification and Subsequent Biofunctionalization of Porous Anodic Alumina Using Terminal Alkynes. *Langmuir* **2011**, *27*, 13606−13617.

(7) Yao, L.; Zheng, M.; Li, H.; Ma, L.; Shen, W. High-Performance Humidity Sensors Based on High-Field Anodized Porous Alumina Films. *Nanotechnology* **2009**, *20*, 395501.

(8) Fröhlich, K.; Hojati-Talemi, P.; Bishop, M.; Zuber, K.; Murphy, P.; Evans, D. Large Area Nanostructured Arrays: Optical Properties of Metallic Nanotubes. *ACS Appl. Mater. Interfaces* **2013**, *5*, 3937−3942.

(9) Buijnsters, J. G.; Zhong, R.; Tsyntsaru, N.; Celis, J.-P. Surface Wettability of Macroporous Anodized Aluminum Oxide. *ACS Appl. Mater. Interfaces* **2013**, *5*, 3224−3233.

(10) Han, H.; Park, S.-J.; Jang, J. S.; Ryu, H.; Kim, K. J.; Baik, S.; Lee, W. In Situ Determination of the Pore Opening Point during Wet-Chemical Etching of the Barrier Layer of Porous Anodic Aluminum Oxide: Nonuniform Impurity Distribution in Anodic Oxide. *ACS Appl. Mater. Interfaces* **2013**, *5*, 3441−3448.

(11) Li, D.; Jiang, C.; Jiang, J.; Lu, J. G. Self-Assembly of Periodic Serrated Nanostructures. *Chem. Mater.* **2009**, *21*, 253−258.

(12) Parkhutik, V. P.; Shershulsky, V. I. Theoretical Modeling of Porous Oxide-Growth on Aluminum. *J. Phys. D: Appl. Phys.* **1992**, *25*, 1258−1263.

(13) Thompson, G. E. Porous Anodic Alumina: Fabrication, Characterization and Applications. *Thin Solid Films* **1997**, *297*, 192−201.

(14) Garcia-Vergara, S. J.; Skeldon, P.; Thompson, G. E.; Habazaki, H. A Flow Model of Porous Anodic Film Growth on Aluminium. *Electrochim. Acta* **2006**, *52*, 681−687.

(15) Houser, J. E.; Hebert, K. R. The Role of Viscous Flow of Oxide in the Growth of Self-Ordered Porous Anodic Alumina Films. *Nat. Mater.* **2009**, *8*, 415−420.

(16) Zhu, X.-F.; Song, Y.; Liu, L.; Wang, C.-Y.; Zheng, J.; Jia, H.-B.; Wang, X.-L. Electronic Currents and the Formation of Nanopores in Porous Anodic Alumina. *Nanotechnology* **2009**, *20*, 475303.

(17) Zhu, X.; Song, Y.; Yu, D.; Zhang, C.; Yao, W. A Novel Nanostructure Fabricated by an Improved Two-step Anodizing Technology. *Electrochem. Commun.* **2013**, *29*, 71−74.

(18) Li, F.; Zhang, L.; Metzger, R. M. On the Growth of Highly Ordered Pores in Anodized Aluminum Oxide. *Chem. Mater.* **1998**, *10*, 2470−2480.

(19) Diggle, J. W.; Downie, T. C.; Goulding, C. W. Anodic Oxide Films on Aluminum. *Chem. Rev.* **1969**, *69*, 365−405.

(20) Masuda, H.; Asoh, H.; Watanabe, M.; Nishio, K.; Nakao, M.; Tamamura, T. Square and Triangular Nanohole Array Architectures in Anodic Alumina. *Adv. Mater.* **2001**, *13*, 189−192.

(21) Leung, S.-F.; Yu, M.; Lin, Q.; Kwon, K.; Ching, K.-L.; Gu, L.; Yu, K.; Fan, Z. Efficient Photon Capturing with Ordered Three-Dimensional Nanowell Arrays. *Nano Lett.* **2012**, *12*, 3682−3689.

(22) Lin, Q.; Leung, S.-F.; Tsui, K.-H.; Hua, B.; Fan, Z. Programmable Nanoengineering Templates for Fabrication of Three-Dimensional Nanophotonic Structures. *Nanoscale Res. Lett.* **2013**, *8*, 268.

(23) Lin, Q.; Hua, B.; Leung, S.-f.; Duan, X.; Fan, Z. Efficient Light Absorption with Integrated Nanopillar/Nanowell Arrays for Three-Dimensional Thin-Film Photovoltaic Applications. *ACS Nano* **2013**, *7*, 2725−2732.

(24) Yu, R.; Ching, K.-L.; Lin, Q.; Leung, S.-F.; Arcrossito, D.; Fan, Z. Strong Light Absorption of Self-Organized 3-D Nanospike Arrays for Photovoltaic Applications. *ACS Nano* **2011**, *5*, 9291−9298.

(25) Mazzarolo, A.; Lee, K.; Vicenzo, A.; Schmuki, P. Anodic TiO_2 Nanotubes: Influence of Top Morphology on Their Photocatalytic Performance. *Electrochem. Commun.* **2012**, *22*, 162−165.

(26) Lee, W.; Ji, R.; Gösele, U.; Nielsch, K. Fast Fabrication of Long-Range Ordered Porous Alumina Membranes by Hard Anodization. *Nat. Mater.* **2006**, *5*, 741−747.

(27) Ono, S.; Saito, M.; Ishiguro, M.; Asoh, H. Controlling Factor of Self-Ordering of Anodic Porous Alumina. *J. Electrochem. Soc.* **2004**, *151*, B473−B478.

(28) Yang, R.; Jiang, L.; Zhu, X.; Song, Y.; Yu, D.; Han, A. Theoretical Derivation of Ionic Current and Electronic Current and Comparison between Fitting Curves and Measured Curves. *RSC Adv.* **2012**, *2*, 12474−12481.

(29) Zhong, X.; Yu, D.; Zhang, S.; Chen, X.; Song, Y.; Li, D.; Zhu, X. Fabrication and Formation Mechanism of Triple-Layered TiO_2 Nanotubes. *J. Electrochem. Soc.* **2013**, *160*, E125−E129.

(30) Chu, S. Z.; Wada, K.; Inoue, S.; Isogai, M.; Katsuta, Y.; Yasumori, A. Large-Scale Fabrication of Ordered Nanoporous Alumina

Films with Arbitrary Pore Intervals by Critical-Potential Anodization. *J. Electrochem. Soc.* **2006**, *153*, B384−B391.
(31) Li, A. P.; Muller, F.; Birner, A.; Nielsch, K.; Gosele, U. Hexagonal Pore Arrays with a 50-420 nm Interpore Distance Formed by Self-Organization in Anodic Alumina. *J. Appl. Phys.* **1998**, *84*, 6023−6026.
(32) Ono, S.; Saito, M.; Asoh, H. Self-ordering of Anodic Porous Alumina Induced by Local Current Concentration: Burning. *Electrochem. Solid-State Lett.* **2004**, *7*, B21−B24.
(33) Duffy, D. C.; McDonald, J. C.; Schueller, O. J. A.; Whitesides, G. M. Rapid Prototyping of Microfluidic Systems in Poly(dimethylsiloxane). *Anal. Chem.* **1998**, *70*, 4974−4984.
(34) Morra, M.; Occhiello, E.; Marola, R.; Garbassi, F.; Humphrey, P.; Johnson, D. On the Aging of Oxygen Plasma-Treated Polydimethylsiloxane Surfaces. *J. Colloid Interface Sci.* **1990**, *137*, 11−24.
(35) Kim, J.; Chaudhury, M. K.; Owen, M. J.; Orbeck, T. The Mechanisms of Hydrophobic Recovery of Polydimethylsiloxane Elastomers Exposed to Partial Electrical Discharges. *J. Colloid Interface Sci.* **2001**, *244*, 200−207.
(36) Cassie, A. B. D.; Baxter, S. Wettability of Porous Surfaces. *Trans. Faraday Soc.* **1944**, *40*, 0546−0550.
(37) Extrand, C. W. Criteria for Ultralyophobic Surfaces. *Langmuir* **2004**, *20*, 5013−5018.
(38) Wenzel, R. N. Resistance of Solid Surfaces to Wetting by Water. *Ind. Eng. Chem.* **1936**, *28*, 988−994.
(39) Odom, T. W.; Love, J. C.; Wolfe, D. B.; Paul, K. E.; Whitesides, G. M. Improved Pattern Transfer in Soft Lithography Using Composite Stamps. *Langmuir* **2002**, *18*, 5314−5320.
(40) Shirtcliffe, N. J.; McHale, G.; Newton, M. I.; Chabrol, G.; Perry, C. C. Dual-Scale Roughness Produces Unusually Water-Repellent Surfaces. *Adv. Mater.* **2004**, *16*, 1929−1932.